



# Lysine-aided PMMA-templating preparation and high performance of three-dimensionally ordered macroporous $\text{LaMnO}_3$ with mesoporous walls for the catalytic combustion of toluene

Yuxi Liu<sup>a</sup>, Hongxing Dai<sup>a,\*</sup>, Yucheng Du<sup>b</sup>, Jiguang Deng<sup>a</sup>, Lei Zhang<sup>a</sup>, Zhenxuan Zhao<sup>a</sup>

<sup>a</sup> Laboratory of Catalysis Chemistry and Nanoscience, Department of Chemistry and Chemical Engineering, College of Environmental and Energy Engineering, Beijing University of Technology, Beijing 100124, China

<sup>b</sup> Key Lab of Advanced Functional Materials, Ministry of Education, College of Materials Science and Engineering, Beijing University of Technology, Beijing 100124, China

## ARTICLE INFO

### Article history:

Received 30 December 2011

Accepted 10 February 2012

Available online 17 February 2012

### Keywords:

Surfactant-assisted poly(methyl methacrylate)-templating method  
Three-dimensionally ordered macroporous perovskite-type oxide  
Lanthanum manganite  
Mesoporous skeletons  
Toluene combustion

## ABSTRACT

Rhombohedrally crystallized three-dimensionally ordered macroporous (3DOM) perovskite-type oxides  $\text{LaMnO}_3$  with mesoporous skeletons were prepared using the poly(ethylene glycol) (PEG)- and/or L-lysine-assisted poly(methyl methacrylate) (PMMA)-templating method. Physicochemical properties of the materials were characterized by numerous analytical techniques. Catalytic performance of the as-prepared  $\text{LaMnO}_3$  samples was evaluated for the combustion of toluene. It is found that addition of appropriate amounts of PEG400 and L-lysine was beneficial for the generation of high-quality 3DOM-structured  $\text{LaMnO}_3$  (denoted as  $\text{LaMnO}_3\text{-PL-1}$ ,  $\text{LaMnO}_3\text{-PL-2}$ , and  $\text{LaMnO}_3\text{-PL-3}$  derived with a PEG400/L-lysine molar ratio of 1.23, 0.61, and 0.31, respectively) with mesoporous skeletons and high surface areas (32–38  $\text{m}^2/\text{g}$ ). Among the  $\text{LaMnO}_3$  samples, the  $\text{LaMnO}_3\text{-PL-2}$  one possessed the largest surface area and the highest contents of surface  $\text{Mn}^{4+}$  and adsorbed oxygen species. 3DOM-structured  $\text{LaMnO}_3$  showed better low-temperature reducibility than bulk  $\text{LaMnO}_3$ , with the  $\text{LaMnO}_3\text{-PL-2}$  sample displaying the best low-temperature reducibility. Under the conditions of toluene concentration = 1000 ppm, toluene/ $\text{O}_2$  molar ratio = 1/400, and space velocity = 20,000  $\text{mL}/(\text{g h})$ , the porous  $\text{LaMnO}_3$  catalysts remarkably outperformed the nonporous bulk counterpart; over the best-performing  $\text{LaMnO}_3\text{-PL-2}$  catalyst, the temperatures required for toluene conversion = 50 and 90% were ca. 226 and 249  $^\circ\text{C}$ , respectively. The apparent activation energies (58–61  $\text{kJ}/\text{mol}$ ) for toluene combustion over the  $\text{LaMnO}_3\text{-PL-1-3}$  catalysts were much lower than that (97  $\text{kJ}/\text{mol}$ ) over the bulk  $\text{LaMnO}_3$  catalyst. It is concluded that the large surface area, high oxygen adspecies content, good low-temperature reducibility, and unique bimodal pore structure were responsible for the good performance of 3DOM-architected  $\text{LaMnO}_3$  with mesoporous skeletons for toluene combustion.

© 2012 Elsevier B.V. All rights reserved.

## 1. Introduction

Most of the volatile organic compounds (VOCs) emitted from industrial and transportation activities are harmful to the atmosphere and human health [1]. With the promulgation of increasingly stringent regulations for VOC emission control, it is urgent to develop effective strategies for the removal of VOCs. Catalytic combustion is believed to be one of the most efficient pathways in eliminating VOCs. The key issue of such a process is the availability of an effective catalyst. Among the catalysts investigated so far, supported precious metals exhibit the best performance in catalyzing the complete oxidation of organics, but the

high cost limits their wide applications. Therefore, cheap metal oxides that show good performance are highly welcomed.

Perovskite-type oxides ( $\text{ABO}_3$ ) are a kind of catalysts active for the combustion of VOCs at high temperatures [2,3], but their low-temperature catalytic activities are inferior to those of noble metals [4,5]. Among the  $\text{ABO}_3$  catalysts, the cobaltite and manganite ones perform the best for the oxidation of organics [6]. For example, an ethanol conversion of 90% could be achieved over the  $\text{LaMnO}_3$  catalyst at a temperature of ca. 202  $^\circ\text{C}$  and a space velocity (SV) of 60,000  $\text{mL}/(\text{g h})$  [7]. Over the  $\text{LaMnO}_3$  catalyst at ca. 335  $^\circ\text{C}$  and 14,000  $\text{h}^{-1}$ , 90% benzene conversion could be obtained [8]. After examining the catalytic activity of  $\text{LaMnO}_3$  for toluene combustion, Irusta et al. [9] found that 90% toluene conversion was reached at ca. 290  $^\circ\text{C}$  and 178  $\text{h}^{-1}$ . Over the  $\text{LaMnO}_{3,12}$  nanoparticles under the conditions of temperature = 295  $^\circ\text{C}$  and SV = 20,000  $\text{h}^{-1}$ , a toluene conversion of 80% was observed [10].

\* Corresponding author. Tel.: +86 10 6739 6118; fax: +86 10 6739 1983.  
E-mail address: [hxdai@bjut.edu.cn](mailto:hxdai@bjut.edu.cn) (H. Dai).

It has been generally accepted that catalytic activity of an  $\text{ABO}_3$  is associated with surface area, pore structure, oxygen non-stoichiometry, and reducibility. These factors are determined by the preparation method adopted. The preservation of high surface area is critical because the reaction rate has often been observed to be directly proportional to the surface area of a bulk perovskite catalyst, especially in the case of combustion of hydrocarbons and oxygenates. The  $\text{ABO}_3$  materials derived from the hydrothermal [10], sol–gel [11], co-precipitation [12], and solid-state reaction [13] routes are usually nonporous and possess relatively low surface areas ( $<10\text{ m}^2/\text{g}$ ), which are unfavorable for the facile accessibility of reactant molecules to active sites. Hence, it is highly desired to establish an effective method for the controlled preparation of  $\text{ABO}_3$  with porous structures and high surface areas. Unfortunately, only several reports on the successful preparation of ordered macro- or mesoporous perovskite-type oxides have been so far seen in the literature. With the aid of block copolymer Pluronic PE 10300, Hou et al. [14] fabricated nanoporous  $\text{BaTiO}_3$  with a surface area of  $70\text{ m}^2/\text{g}$ . Via the evaporation-induced self-assembling route, Fan et al. [15] prepared mesoporous  $\text{SrTiO}_3$  and  $\text{BaTiO}_3$  that possessed a surface area of 206 and  $167\text{ m}^2/\text{g}$ , respectively. Using metal nitrates or acetates as precursors and well-aligned polymethyl methacrylate (PMMA) or polystyrene microspheres as hard template, 3DOM-structured  $\text{La}_{1-x}\text{Sr}_x\text{FeO}_3$  (surface area =  $24\text{--}49\text{ m}^2/\text{g}$ ) [16],  $\text{LaMnO}_3$  [17], and  $\text{La}_{0.7}\text{Ca}_{0.3-x}\text{Sr}_x\text{MnO}_3$  (ca.  $24\text{ m}^2/\text{g}$ ) [18] were prepared. Zhao et al. adopted PMMA as template to generate 3DOM-structured  $\text{LaFeO}_3$ -supported Au (surface area = ca.  $32\text{ m}^2/\text{g}$ ) [19] and  $\text{LaCo}_x\text{Fe}_{1-x}\text{O}_3$  ( $x=0\text{--}0.5$ ) [20] catalysts, which showed super performance for the catalytic oxidation of soot. Recently, Wang et al. [21] synthesized ordered mesoporous  $\text{LaCoO}_3$  with a surface area of ca.  $97\text{ m}^2/\text{g}$  through an ordered mesoporous silica (KIT-6)-nanocasting pathway.

In the past years, our group have investigated the controlled preparation and physicochemical properties of high-surface-area  $\text{MgO}$  [22],  $\text{CaO}$  [23],  $\gamma\text{-Al}_2\text{O}_3$  [24],  $\alpha\text{-Fe}_2\text{O}_3$  [25], and  $\text{BiVO}_4$  [26] by using the surfactant-templating [22,23,26] or surfactant-assisted PMMA-templating [24,25] strategy. We found that addition of a surfactant was beneficial for the generation of mesoporous or nanovoid-like structures and hence for the improvement in physicochemical property [22–26]. To the best of our knowledge, however, there have been no reports on the successful preparation of 3DOM-structured perovskite-type oxides with mesoporous or nanovoid-like skeletons and their application in catalyzing the combustion of VOCs. In this paper, we report the L-lysine-assisted PMMA-templating preparation, characterization, and catalytic activities of 3DOM-structured  $\text{LaMnO}_3$  with mesoporous skeletons for the complete oxidation of toluene. It is observed that the bimodal porous perovskite materials showed good catalytic performance for the addressed reaction.

## 2. Experimental

### 2.1. Catalyst preparation

The well-aligned hard template PMMA microspheres with an average diameter of ca. 300 nm (Fig. S1 of the Supplementary data) were synthesized according to the procedures described elsewhere [24].

The 3DOM  $\text{LaMnO}_3$  samples with mesoporous skeletons were prepared using the surfactant-assisted PMMA-templating strategy. In a typical procedure, the stoichiometric amounts of  $\text{La}(\text{NO}_3)_3 \cdot 6\text{H}_2\text{O}$  and  $\text{Mn}(\text{NO}_3)_2$  (50 wt% aqueous solution) were dissolved in 3 mL of PEG with a molecular weight of 400 g/mol and 3 mL of methanol (MeOH) at room temperature (RT) under stirring

for 4 h to obtain a transparent solution. 1.00, 2.00 or 4.00 g of L-lysine was dissolved in a  $\text{HNO}_3$  aqueous solution (5 mol/L), and the pH value of this solution was adjusted to ca. 6 for avoiding the formation of metal hydroxide precipitates in the following steps. Then, the L-lysine-containing solution was mixed with the metal nitrate-containing transparent solution under stirring for 1 h to obtain a uniform precursor solution, to which a certain amount of MeOH was added to achieve a total metal concentration of 2 mol/L. Circa 2.0 g of the PMMA hard template was soaked in the above precursor solution for 4 h. After being filtered, the obtained wet PMMA template was dried in air at RT for 48 h, and then transferred to a ceramic boat which was placed in a tubular furnace. The thermal treatment process was divided into two steps: (i) the solid was first calcined in a  $\text{N}_2$  flow of 50 mL/min at a ramp of  $1^\circ\text{C}/\text{min}$  from RT to  $300^\circ\text{C}$  and kept at this temperature for 3 h, and then cooled to  $50^\circ\text{C}$  in the same atmosphere; and (ii) after being purged in an air flow of 50 mL/min, the solid was heated in the same atmosphere at a ramp of  $1^\circ\text{C}/\text{min}$  from RT to  $300^\circ\text{C}$  and held at  $300^\circ\text{C}$  for 2 h, and then was calcined continuously at the same ramp from 300 to  $750^\circ\text{C}$  and maintained at  $750^\circ\text{C}$  for 4 h. The 3DOM-structured sample obtained with 1.00, 2.00, and 4.00 g of L-lysine was denoted as  $\text{LaMnO}_3\text{-PL-1}$ ,  $\text{LaMnO}_3\text{-PL-2}$ , and  $\text{LaMnO}_3\text{-PL-3}$ , respectively, in which the “PL” represents the “PMMA” and “L-lysine”. In order to examine the effect of calcination temperature on the pore structure, we calcined the  $\text{LaMnO}_3\text{-PL-2}$  sample at 850 or  $950^\circ\text{C}$ , thus obtaining the  $\text{LaMnO}_3\text{-PL-2.850}$  and  $\text{LaMnO}_3\text{-PL-2.950}$  samples, respectively.

For comparison purposes, several  $\text{LaMnO}_3$  samples were also prepared. When no surfactant L-lysine was added but other parameters and calcination procedures were the same as those adopted for the preparation of  $\text{LaMnO}_3\text{-PL-1–3}$ , a 3DOM  $\text{LaMnO}_3$  sample (denoted as  $\text{LaMnO}_3\text{-PEG}$ ) was obtained. By using the same method in the absence of surfactant L-lysine and PEG, a 3DOM  $\text{LaMnO}_3$  sample (denoted as  $\text{LaMnO}_3\text{-MeOH}$ ) was generated. The bulk  $\text{LaMnO}_3$  sample was prepared via the citric acid-complexing route [11] and after calcination in air at  $850^\circ\text{C}$  for 4 h. For the sake of better presentation, the main preparation conditions of these  $\text{LaMnO}_3$  materials are summarized in Table 1.

All of the chemicals (A.R. in purity) were purchased from Beijing Chemical Company and used without further purification.

### 2.2. Catalyst characterization

The catalysts were characterized using the techniques of X-ray diffraction (XRD), thermogravimetric analysis (TGA) and differential scanning calorimetry (DSC), Fourier-transform infrared (FT-IR) spectroscopy,  $\text{N}_2$  adsorption–desorption (BET), scanning electron microscopy (SEM), transmission electron microscopy (TEM), high-resolution TEM, selected-area electron diffraction (SAED), and X-ray photoelectron spectroscopy (XPS). The detailed procedures were described in Supplementary data.

Hydrogen temperature-programmed reduction ( $\text{H}_2\text{-TPR}$ ) experiments were carried out on a chemical adsorption analyzer (Autochem II 2920, Micromeritics). Before TPR measurement, ca. 0.02 g of catalyst (40–60 mesh) was loaded to a fixed-bed U-shaped quartz microreactor (i.d. = 4 mm) and pretreated in an  $\text{O}_2$  flow of 30 mL/min at  $500^\circ\text{C}$  for 1 h. After being cooled at the same atmosphere to RT, the pretreated sample was exposed to a flow (50 mL/min) of 5%  $\text{H}_2$ –95% Ar (v/v) mixture and heated from RT to  $900^\circ\text{C}$  at a ramp of  $10^\circ\text{C}/\text{min}$ . The alteration in  $\text{H}_2$  concentration of the effluent was monitored on-line by the chemical adsorption analyzer. The reduction peak was calibrated against that of the complete reduction of a known standard of powdered CuO (Aldrich, 99.995%).

**Table 1**  
Preparation conditions, crystallite sizes, BET surface areas, average pore sizes, and pore volumes of the as-obtained LaMnO<sub>3</sub> samples.

Catalyst code	Hard template/surfactant	(La + Mn)/L-lysine molar ratio (mol/mol)	PEG400/L-lysine molar ratio (mol/mol)	Calcination condition	Crystallite size <sup>a</sup> (nm)	BET surface area (m <sup>2</sup> /g)		Pore volume (cm <sup>3</sup> /g)	Average pore size (nm)	
						Macropore (>50 nm)	Mesopore (≤50 nm)		Macropore <sup>b</sup> (>50 nm)	Mesopore <sup>b</sup> (≤50 nm)
LaMnO <sub>3</sub> -bulk	—	—	—	850 °C 4 h (in air)	118	—	7.3	—	—	—
LaMnO <sub>3</sub> -MeOH	PMMA/—	—	—	300 °C 3 h (in N <sub>2</sub> ) → 300 °C 2 h (in air) → 750 °C 4 h (in air)	31	1.6	19.8	0.062	135	7.5
LaMnO <sub>3</sub> -PEG	PMMA/PEG400	—	—	300 °C 3 h (in N <sub>2</sub> ) → 300 °C 2 h (in air) → 750 °C 4 h (in air)	37	6.4	25.5	0.093	140	13.9
LaMnO <sub>3</sub> -PL-1	PMMA/(L-lysine + PEG400)	8.8	1.23/1	300 °C 3 h (in N <sub>2</sub> ) → 300 °C 2 h (in air) → 750 °C 4 h (in air)	38	5.2	31.2	0.096	120	11.8
LaMnO <sub>3</sub> -PL-2	PMMA/(L-lysine + PEG400)	4.4	0.61/1	300 °C 3 h (in N <sub>2</sub> ) → 300 °C 2 h (in air) → 750 °C 4 h (in air)	33	3.5	34.3	0.085	110	10.7
LaMnO <sub>3</sub> -PL-3	PMMA/(L-lysine + PEG400)	2.2	0.31/1	300 °C 3 h (in N <sub>2</sub> ) → 300 °C 2 h (in air) → 750 °C 4 h (in air)	30	2.2	30.1	0.065	85	8.3
LaMnO <sub>3</sub> -PL-2.850	PMMA/(L-lysine + PEG400)	4.4	0.61/1	300 °C 3 h (in N <sub>2</sub> ) → 300 °C 2 h (in air) → 850 °C 4 h (in air)	60	2.3	16.5	0.058	80	8.7
LaMnO <sub>3</sub> -PL-2.950	PMMA/(L-lysine + PEG400)	4.4	0.61/1	300 °C 3 h (in N <sub>2</sub> ) → 300 °C 2 h (in air) → 950 °C 4 h (in air)	124	1.1	9.0	0.027	65	8.8

<sup>a</sup> Data calculated according to the full width at half-maximum of the (110) XRD line and the Scherrer equation.

<sup>b</sup> Estimated according to the SEM and TEM images.

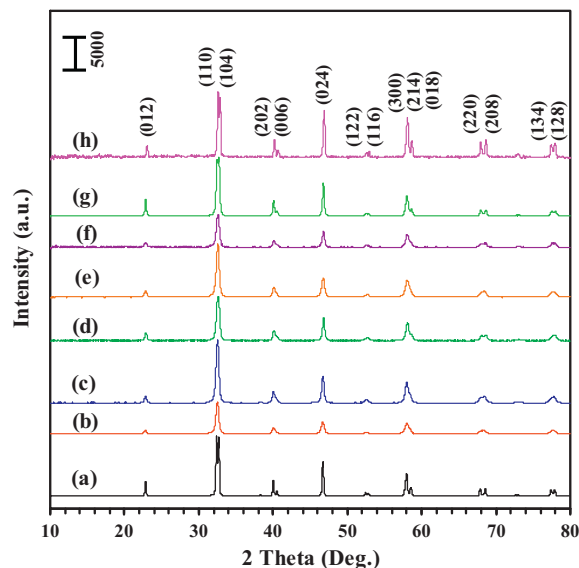


**Fig. 1.** XRD patterns of (a) LaMnO<sub>3</sub>-bulk, (b) LaMnO<sub>3</sub>-MeOH, (c) LaMnO<sub>3</sub>-PEG, (d) LaMnO<sub>3</sub>-PL-1, (e) LaMnO<sub>3</sub>-PL-2, (f) LaMnO<sub>3</sub>-PL-3, (g) LaMnO<sub>3</sub>-PL-2.850, and (h) LaMnO<sub>3</sub>-PL-2.950.

### 2.3. Catalytic activity measurement

A continuous flow fixed-bed quartz microreactor (i.d. = 4 mm) was used to measure the catalytic activities of the samples at atmospheric pressure for the complete oxidation of toluene. To minimize the effect of hot spots, 0.1 g of the catalyst sample (40–60 mesh) was diluted with 0.3 g of quartz sands (40–60 mesh). The total flow rate of the reactant mixture (1000 ppm toluene + O<sub>2</sub> + N<sub>2</sub> (balance)) was 33.3 mL/min, giving a toluene/O<sub>2</sub> molar ratio of 1/400 and a SV of 20,000 mL/(g h). The 1000-ppm toluene was generated by passing a N<sub>2</sub> flow through a bottle containing pure toluene (A.R. grade) chilled in an ice-water isothermal bath. For the changes of SV and toluene/O<sub>2</sub> molar ratio, we altered the total mass flow of feed gas mixture and the mass flow of O<sub>2</sub>, respectively. Reactants and products were analyzed on-line by a gas chromatograph (GC-2010, Shimadzu) equipped with a flame ionization detector (FID) and a thermal conductivity detector (TCD), using a 1/8 in Chromosorb 101 column (3 m in length) for VOCs separation and a 1/8 in Carboxen 1000 column (3 m in length) for permanent gas separation. The balance of carbon throughout the investigation was estimated to be 99.5%.

## 3. Results and discussion

### 3.1. Crystal phase composition

Fig. 1 shows the XRD patterns of the as-prepared LaMnO<sub>3</sub> samples. By comparing the XRD pattern of the standard LaMnO<sub>3</sub> sample (JCPDS PDF# 82-1152), one can realize that the XRD peaks of each as-prepared sample in the 2θ range of 10–80° could be well indexed, as indicated in Fig. 1(h) and Fig. S2. In other words, all of the LaMnO<sub>3</sub> samples were single-phase and of a rhombohedral crystal structure. It is known that the crystal phase (orthorhombic, rhombohedral or monoclinic) of LaMnO<sub>3</sub> is strongly dependent on the preparation condition [27]. By adopting various preparation approaches under different calcination conditions, rhombohedral LaMnO<sub>3</sub> [28–33] and hexagonal LaMnO<sub>3</sub> [34–37] could be generated. From Fig. 1, one can also observe that there were differences in peak intensities of the eight samples, suggesting the presence of discrepancies in LaMnO<sub>3</sub> crystallinity, a result due to the various preparation conditions adopted. With the rise

in calcination temperature from 750 to 850 or 950 °C, the obtained  $\text{LaMnO}_3$ -PL-2.850 and  $\text{LaMnO}_3$ -PL-2.950 as well as the  $\text{LaMnO}_3$ -bulk (calcined at 850 °C) samples displayed improved crystallinity. As can be seen from Table 1, the crystallite size (118 nm) of  $\text{LaMnO}_3$ -bulk was much larger than those (30–38 nm) of  $\text{LaMnO}_3$ -MeOH,  $\text{LaMnO}_3$ -PEG, and  $\text{LaMnO}_3$ -PL-1–3; moreover, the rise in calcination temperature from 750 to 850 or 950 °C, the crystallite size of  $\text{LaMnO}_3$ -PL-2 increased significantly from 33 to 60 or 124 nm. The results of TGA/DSC and FT-IR investigations (Figs. S3 and S4, respectively) substantiate that the organic species retained in the uncalcined samples were totally removed after thermal treatments first in a  $\text{N}_2$  flow and then in an air flow at or above 750 °C. The formation of single-phase rhombohedral perovskite structure in each of the  $\text{LaMnO}_3$  samples demonstrates that the calcination temperature of 750 °C was appropriate.

### 3.2. Morphology, pore structure, and surface area

Figs. 2 and 3 show the representative SEM and TEM images as well as the SAED patterns of the as-prepared  $\text{LaMnO}_3$  samples, respectively. It is observed that after calcination at 750 °C, all of the samples displayed a 3DOM architecture but their qualities were different. The  $\text{LaMnO}_3$ -MeOH sample derived in the absence of PEG400 and L-lysine showed a poor 3DOM structure with an average pore size of ca. 135 nm. With the introduction of PEG400 and/or L-lysine, high-quality 3DOM structures were formed in the  $\text{LaMnO}_3$ -PEG and  $\text{LaMnO}_3$ -PL-1–3 samples with a pore-size range of 85–140 nm. The macropore shapes and skeleton thickness of these 3DOM-structured materials were different due to the differences in preparation conditions and thermal treatment temperature. Obviously, the skeleton thickness of  $\text{LaMnO}_3$ -PL-2 increased significantly when the calcination temperature rose. Ueda et al. [38] obtained 3DOM-structured  $\text{LaFeO}_3$  with nanovoids in the macropore walls in the presence of MeOH and ethylene glycol, in which ethylene glycol would play a key role in forming nanovoids in the skeletons of 3DOM  $\text{LaFeO}_3$ . In our  $\text{LaMnO}_3$ -PEG sample derived with MeOH and PEG400, however, no nanovoids or mesopores in the  $\text{LaMnO}_3$ -PEG skeletons were observed. With the addition of L-lysine, the obtained  $\text{LaMnO}_3$ -PL-1–3 samples possessed a large number of mesopores scattering in the skeletons of macropores, but the mesopore structure of  $\text{LaMnO}_3$ -PL-2 was markedly destroyed when the calcination temperature increased from 750 to 850 or 950 °C, a result due to the growth of nanocrystallites at high temperatures. The mesopore diameters of these bimodal porous materials were in the range of 2–8 nm. From the high-resolution TEM images, one can also estimate the lattice spacings of the (110) crystal plane of the  $\text{LaMnO}_3$  samples to be 0.275–0.276 nm, rather close to that (0.27644 nm) for the (110) crystal plane of the standard rhombohedrally crystallized  $\text{LaMnO}_3$  sample (JCPDS PDF# 82-1152). The recording of multiple electron diffraction rings in the SAED patterns (insets of Fig. 3) indicates that these 3DOM-structured  $\text{LaMnO}_3$  samples were polycrystalline. Furthermore, the enhancement in brightness and number of electron diffraction rings with the rise in calcination temperature confirms the improvement in crystallinity of  $\text{LaMnO}_3$ -PL-2.850 and  $\text{LaMnO}_3$ -PL-2.950, as reflected in the XRD investigations (Fig. 1).

Usually, a polymer template (like PMMA or polystyrene microbeads) can function as a support for the conversion of metal precursor(s) to a solid-state framework at low temperatures, and give rise to 3DOM-structured pure or mixed metal oxides after the removal of the polymer template. The glassy transition temperature, decomposition temperature, and oxidation temperature of PMMA in air was ca. 130, 290, and 370 °C [24,39], respectively. The decomposition temperatures of Mn and Co nitrates were close to the glassy transition temperature of PMMA. Solidification due to metal nitrate decomposition would take place concurrently

with the melting of the PMMA, and some of the metal salts were squeezed out from the voids in the polymer template, hence resulting in a low fraction of 3DOM structure. Therefore, it would be difficult to prepare high-quality 3DOM-structured  $\text{LaMnO}_3$  materials if only MeOH was used as solvent. During the calcination process of the PMMA- and PEG400-containing metal nitrates, however, the interaction of the PEG400 and metal nitrates might form solid metal-PEG complexes [16,38] before the melting of the PMMA template, and thus generating the desired 3DOM complex metal oxide intermediates. Adding a certain amount of L-lysine to the metal precursor solutions led to the formation of a number of mesopores in the macropore skeletons, but an excessive amount of L-lysine was unfavorable for the preparation of high-quality 3DOM-structured  $\text{LaMnO}_3$  materials. L-lysine is usually considered as an amino acid-type crystal growth modifier [40,41]. The interaction between amino acid and metal precursors has been well documented in the literature [42,43]. During the preparation process of  $\text{LaMnO}_3$  in the presence of L-lysine, La and Mn ions could interact with the amine functional groups and carboxylate functional groups to form metal-L-lysine complexes. These metal-PEG and/or metal-L-lysine complexes might play a critical role in the generation of mesopores in the macropore skeletons of  $\text{LaMnO}_3$  after the subsequent thermal treatments in various environments. It is worth pointing out that the employment of the calcination procedure (first in  $\text{N}_2$  at 300 °C and then in air at 300 and 750 °C) was essential for 3DOM-structure formation. The PMMA-containing metal precursor was first calcined in  $\text{N}_2$  at 300 °C, possibly causing the PMMA to be partially carbonized, and the formed amorphous carbon could act as a hard template to prevent macro- and mesoporous structure from collapsing before the polymer template was completely oxidized at a higher temperature [44], hence facilitating the retaining of 3DOM-structured  $\text{LaMnO}_3$ .

From the nitrogen adsorption-desorption isotherms of the  $\text{LaMnO}_3$  samples (Fig. 4A), one can see that in addition to the  $\text{LaMnO}_3$ -PL-2.950 sample, the other samples displayed a  $\text{N}_2$  adsorption-desorption isotherm characteristic of a combination of macropore and mesopore structures. The hysteresis loops in the low and high relative pressure ranges were different from sample to sample, indicative of the discrepancy in pore-size distribution. For the  $\text{LaMnO}_3$ -PL-1–3 samples, there was a weak but sharp peak at pore diameter = 2–4 nm (Fig. 4B(c and d) and Fig. S5). In addition to the  $\text{LaMnO}_3$ -PL-2.850 and  $\text{LaMnO}_3$ -PL-2.950 samples, the other samples exhibited a wide pore-size distribution (from 10 to 80 nm), with the  $\text{LaMnO}_3$ -MeOH and  $\text{LaMnO}_3$ -PEG samples showing much wider pore-size distributions than the other samples. It should be noted that there might also be the presence of a small amount of micropores in all of the samples because the  $dV/d(\log(D))$  value decreased with the increase of pore size below 4 nm (Fig. S5). From Table 1, one can observe that the bulk  $\text{LaMnO}_3$  sample exhibited a low surface area (7.3  $\text{m}^2/\text{g}$ ), whereas the 3DOM-structured  $\text{LaMnO}_3$  samples possessed much higher surface areas (21–38  $\text{m}^2/\text{g}$ ). The introduction of PEG or both PEG and L-lysine during the preparation process favored the significant enhancement in surface area (32–38  $\text{m}^2/\text{g}$ ) of the obtained  $\text{LaMnO}_3$  samples, but raising the calcination temperature from 750 to 850 or 950 °C led to a remarkable drop in surface area from 38 to 19 or 10  $\text{m}^2/\text{g}$ , respectively, a result induced by the partial destruction of 3DOM structure and mesopores in the skeletons of the macropores. The pore volumes of all of the  $\text{LaMnO}_3$  samples were relatively low and their average pore sizes were in the range of 8.3–13.9 nm (Table 1).

### 3.3. Surface element composition, surface species, and reducibility

XPS is an effective technique to gain the information related to surface element compositions, metal oxidation states, and adsorbed species of a solid material. Figs. S6 and S7 illustrate the



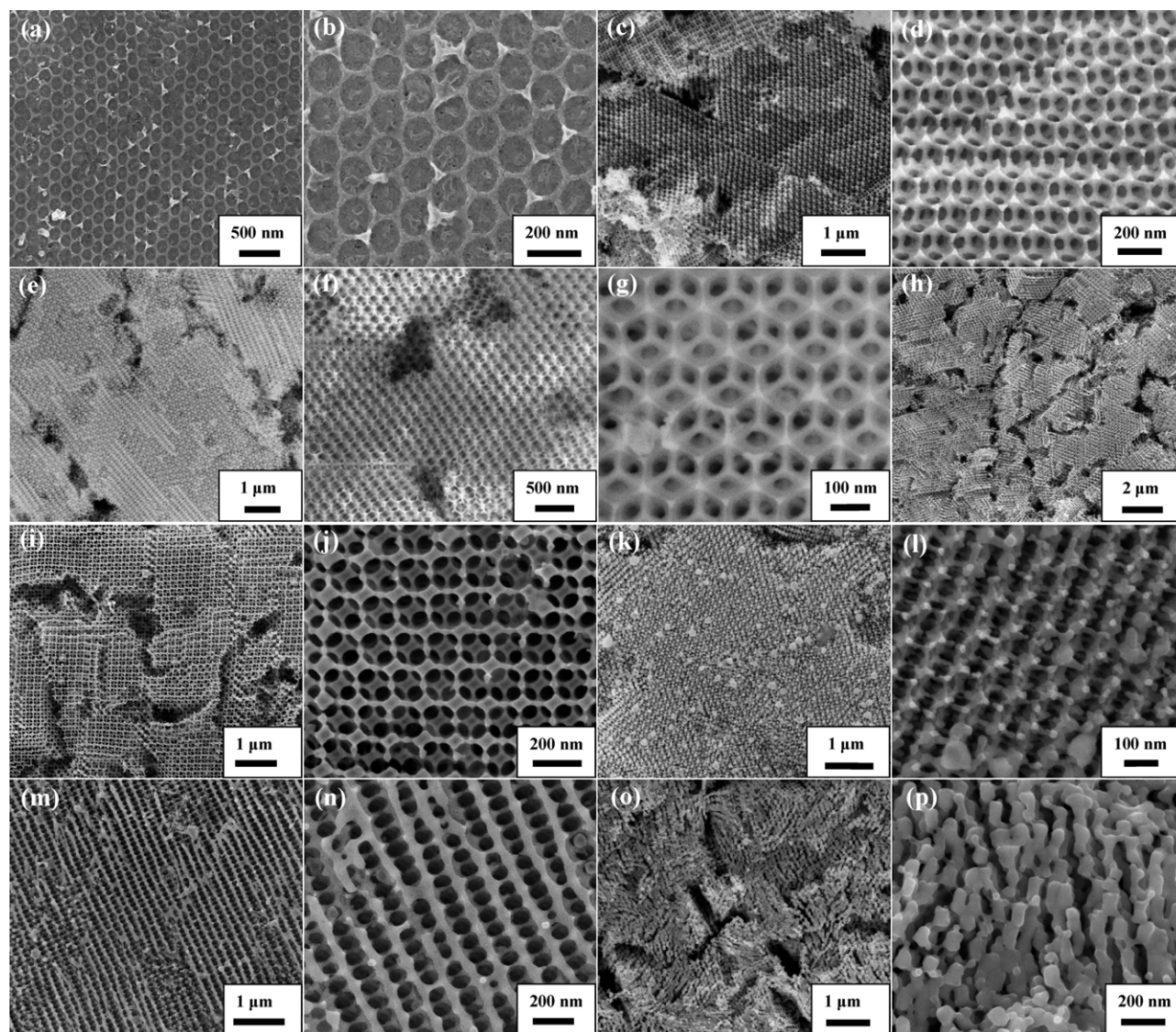


**Fig. 2.** SEM images of (a and b) LaMnO<sub>3</sub>-MeOH, (c and d) LaMnO<sub>3</sub>-PEG, (e–g) LaMnO<sub>3</sub>-PL-1, (h–j) LaMnO<sub>3</sub>-PL-2, (k and l) LaMnO<sub>3</sub>-PL-3, (m and n) LaMnO<sub>3</sub>-PL-2.850, and (o and p) LaMnO<sub>3</sub>-PL-2.950.

Mn 2p<sub>3/2</sub>, O 1s, and C 1s XPS spectra of the LaMnO<sub>3</sub> samples, respectively. It is observed that there was the co-presence of surface Mn<sup>4+</sup> and Mn<sup>3+</sup> species [35,36,45] as well as surface lattice oxygen (O<sub>latt</sub><sup>2-</sup>), adsorbed oxygen (O<sub>ads</sub>, i.e. O<sub>2</sub><sup>-</sup>, O<sub>2</sub><sup>2-</sup> or O<sup>-</sup>) species, and surface carbonates (CO<sub>3</sub><sup>2-</sup>) [12,35,37] on the surfaces of LaMnO<sub>3</sub>

samples. The surface Mn<sup>4+</sup>/Mn<sup>3+</sup> and O<sub>ads</sub>/O<sub>latt</sub><sup>2-</sup> atomic ratios have an important influence on the catalytic performance of manganite. By making quantitative analyses on the XPS spectra, one can estimate the surface element compositions and surface Mn<sup>4+</sup>/Mn<sup>3+</sup> and O<sub>ads</sub>/O<sub>latt</sub><sup>2-</sup> atomic ratios of the LaMnO<sub>3</sub> samples, as

**Table 2**  
Surface element compositions, H<sub>2</sub> consumption, and catalytic activities of the as-prepared LaMnO<sub>3</sub> catalysts under the conditions of toluene concentration = 1000 ppm, toluene/O<sub>2</sub> molar ratio = 1/400, and SV = 20,000 mL/(g h).

Catalyst	Mn/La atomic ratio <sup>a</sup>	Mn/(La + Mn) atomic ratio <sup>a</sup>	O <sub>ads</sub> /O <sub>latt</sub> atomic ratio	Mn <sup>4+</sup> /Mn <sup>3+</sup> atomic ratio	H <sub>2</sub> consumption <sup>b</sup> (mmol/g)		Toluene oxidation activity (°C)		
					<500 °C	>600 °C	T <sub>10%</sub>	T <sub>50%</sub>	T <sub>90%</sub>
LaMnO <sub>3</sub> -bulk	0.99 (1.00)	0.50 (0.50)	0.87	0.80	0.97	2.17	220	267	298
LaMnO <sub>3</sub> -MeOH	0.91 (1.00)	0.48 (0.50)	1.05	0.99	1.45	1.79	201	252	275
LaMnO <sub>3</sub> -PEG	0.93 (1.00)	0.48 (0.50)	1.17	1.44	1.55	1.83	189	241	262
LaMnO <sub>3</sub> -PL-1	1.05 (1.00)	0.51 (0.50)	1.19	1.55	1.84	1.87	180	230	251
LaMnO <sub>3</sub> -PL-2	1.05 (1.00)	0.51 (0.50)	1.31	1.88	1.89	2.27	180	226	249
LaMnO <sub>3</sub> -PL-3	1.04 (1.00)	0.51 (0.50)	1.21	1.64	1.77	1.76	185	240	259
LaMnO <sub>3</sub> -PL-2.850	1.03 (1.00)	0.51 (0.50)	1.13	1.40	1.61	2.18	190	243	268
LaMnO <sub>3</sub> -PL-2.950	1.02 (1.00)	0.50 (0.50)	1.04	0.88	1.38	1.90	200	258	282

<sup>a</sup> The data in parenthesis are the nominal Mn/La or Mn/(La + Mn) atomic ratios in LaMnO<sub>3</sub>.

<sup>b</sup> The data were obtained by quantitatively analyzing the H<sub>2</sub>-TPR profiles.



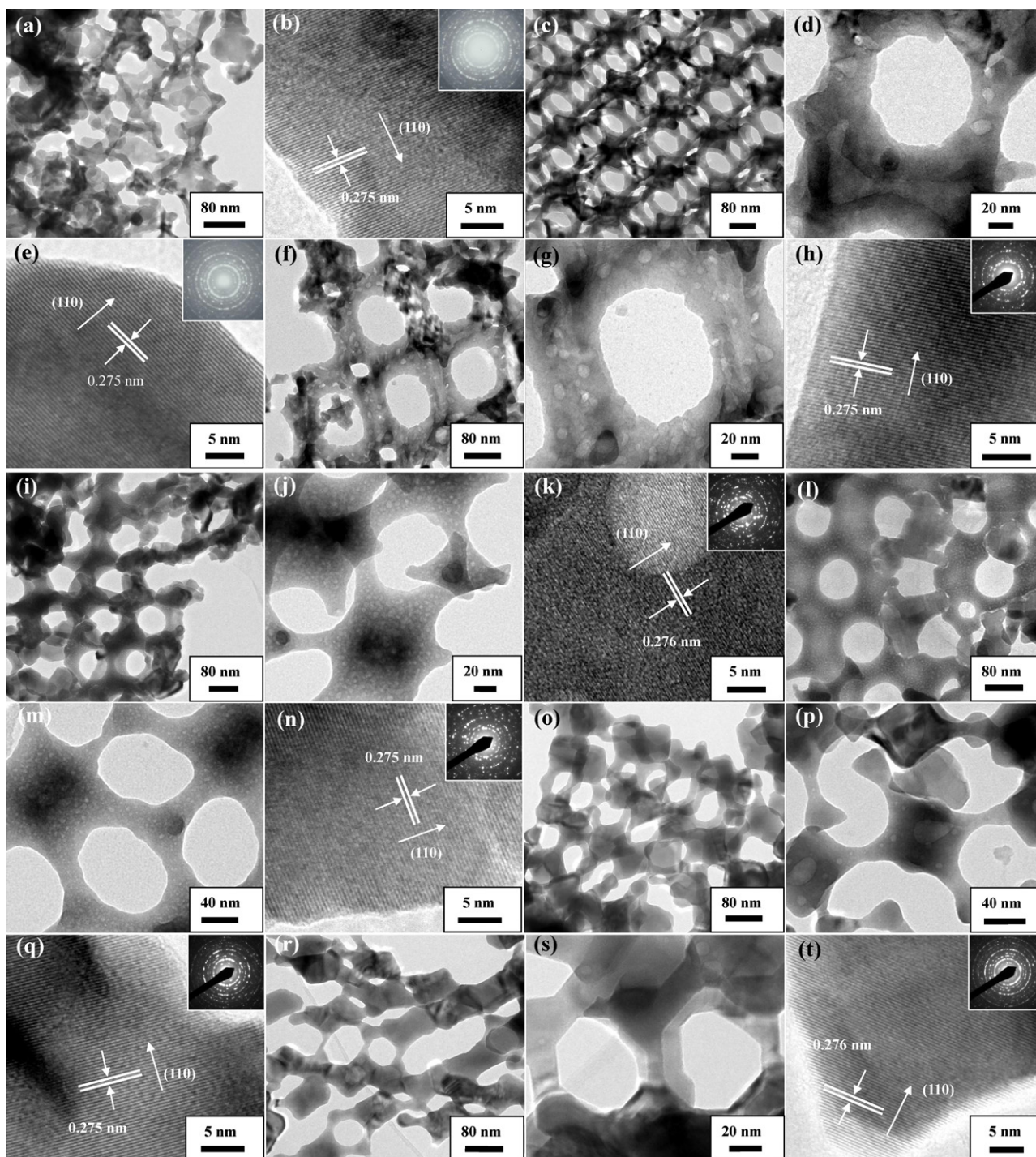


**Fig. 3.** TEM and high-resolution TEM images and SAED patterns (insets) of (a and b)  $\text{LaMnO}_3\text{-MeOH}$ , (c–e)  $\text{LaMnO}_3\text{-PEG}$ , (f–h)  $\text{LaMnO}_3\text{-PL-1}$ , (i–k)  $\text{LaMnO}_3\text{-PL-2}$ , (l–n)  $\text{LaMnO}_3\text{-PL-3}$ , (o–q)  $\text{LaMnO}_3\text{-PL-2.850}$ , and (r–t)  $\text{LaMnO}_3\text{-PL-2.950}$ .

summarized in Table 2. It is found that the surface  $\text{Mn}/\text{La}$  (0.91–0.93) and  $\text{Mn}/(\text{Mn}+\text{La})$  (0.48) atomic ratios of  $\text{LaMnO}_3\text{-MeOH}$  and  $\text{LaMnO}_3\text{-PEG}$  were lower than the corresponding nominal  $\text{Mn}/\text{La}$  (1.00) and  $\text{Mn}/(\text{Mn}+\text{La})$  (0.5) atomic ratios, suggesting the presence of La enrichment on the surfaces of the two samples. The surface  $\text{Mn}/\text{La}$  and  $\text{Mn}/(\text{Mn}+\text{La})$  atomic ratios of the  $\text{LaMnO}_3$  samples derived with PEG and L-lysine were 1.02–1.05 and 0.50–0.51, respectively, slightly higher than the corresponding nominal atomic ratios, indicative of the occurrence of Mn enrichment on the surfaces of these samples. Such phenomena were also observed by other researchers [12]. The discrepancy in

surface  $\text{Mn}^{4+}/\text{Mn}^{3+}$  atomic ratio of these  $\text{LaMnO}_3$  samples was a result due to the different preparation approaches. With the addition of L-lysine, the surface  $\text{Mn}^{4+}/\text{Mn}^{3+}$  atomic ratios (1.55–1.88) of the  $\text{LaMnO}_3\text{-PL}$  samples increased, with the  $\text{LaMnO}_3\text{-PL-2}$  sample exhibiting the highest surface  $\text{Mn}^{4+}/\text{Mn}^{3+}$  atomic ratio (1.88). A rise in calcination temperature, however, led to a drop in surface  $\text{Mn}^{4+}/\text{Mn}^{3+}$  atomic ratio, such a changing trend agreed well with the result reported by Wang et al. [33]. From Table 2, one can observe that among the  $\text{LaMnO}_3$  samples prepared in the present study, the  $\text{LaMnO}_3\text{-PL-2}$  sample showed the highest surface  $\text{O}_{\text{ads}}/\text{O}_{\text{latt}}^{2-}$  atomic ratio (1.31), indicating that a higher surface

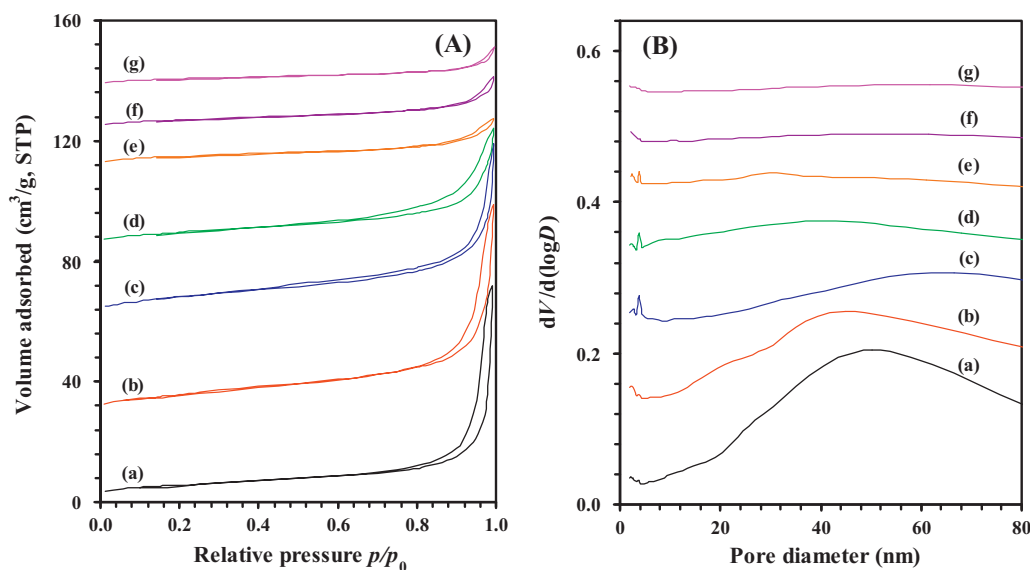


**Fig. 4.** (A) Nitrogen adsorption–desorption isotherms and (B) pore-size distributions of (a)  $\text{LaMnO}_3\text{-MeOH}$ , (b)  $\text{LaMnO}_3\text{-PEG}$ , (c)  $\text{LaMnO}_3\text{-PL-1}$ , (d)  $\text{LaMnO}_3\text{-PL-2}$ , (e)  $\text{LaMnO}_3\text{-PL-3}$ , (f)  $\text{LaMnO}_3\text{-PL-2.850}$ , and (g)  $\text{LaMnO}_3\text{-PL-2.950}$ .

area was beneficial for the enhancement of oxygen adspecies, in good agreement with the result observed in one of our previous works [25]. With the rise in calcination temperature, the amount of surface oxygen species on the  $\text{LaMnO}_3\text{-PL-2}$  sample decreased.

$\text{H}_2\text{-TPR}$  is an ideal tool to examine the reducibility of a solid oxide catalyst. Fig. 5A illustrates the  $\text{H}_2\text{-TPR}$  profiles of the as-prepared  $\text{LaMnO}_3$  samples. The reduction of each sample underwent in two steps: one in the range of 200–500 °C and the other in the range of 600–900 °C. In addition to the bulk  $\text{LaMnO}_3$  sample, the porous  $\text{LaMnO}_3$  samples showed a low-temperature reduction peak at 307–327 °C with a shoulder at 389–418 °C. The reduction peaks at 307–327 °C were due to the reduction of  $\text{Mn}^{4+}$  to  $\text{Mn}^{3+}$  as well as the removal of over-stoichiometric oxygen and oxygen adspecies, and the reduction peaks at 389–418 °C to the single-electron reduction of  $\text{Mn}^{3+}$  located in a coordination-unsaturated microenvironment, whereas the reduction peaks above 600 °C were due to the reduction of the left  $\text{Mn}^{3+}$  to  $\text{Mn}^{2+}$  [35,37,46,47]. The two reduction temperatures (348 and 830 °C) of the bulk  $\text{LaMnO}_3$  sample were much higher than those (307–327 and 702–756 °C) of the porous counterparts, indicating that formation of a porous structure facilitated the reduction of  $\text{LaMnO}_3$ . The  $\text{H}_2\text{-TPR}$  results reveal that the 3DOM-structured  $\text{LaMnO}_3$  samples were more reducible than the bulk  $\text{LaMnO}_3$  sample. Quantitative analyses on the  $\text{H}_2\text{-TPR}$  profiles can give the  $\text{H}_2$  consumption of the samples (Table 2). For the bulk  $\text{LaMnO}_3$  and porous  $\text{LaMnO}_3$  samples, the  $\text{H}_2$  consumption at lower temperatures ( $\leq 600$  °C) was 0.97 and 1.38–1.89 mmol/g, while that at higher temperatures ( $> 600$  °C) was 2.17 and 1.76–2.27 mmol/g, respectively. A large number of works have demonstrated that the amount ( $\delta$ ) of non-stoichiometric excess oxygen accommodated within the lattice of  $\text{LaMnO}_{3+\delta}$  prepared after calcination in air at or above 700 °C falls into the range of 0.12–0.16, which corresponds to a  $\text{H}_2$  consumption of 0.49–0.66 mmol/g below 600 °C. It means that all of the  $\text{Mn}^{4+}$  ions in  $\text{LaMnO}_{3+\delta}$  have been reduced to  $\text{Mn}^{3+}$ . For our  $\text{LaMnO}_3$  catalysts, the  $\text{H}_2$  consumption below 600 °C was in the range of 0.97–1.89 mmol/g, higher than the above values. This result suggests that in addition to the reduction of  $\text{Mn}^{4+}$  to  $\text{Mn}^{3+}$ , there were possible reduction of partial  $\text{Mn}^{3+}$  to  $\text{Mn}^{2+}$  and the removal of oxygen species adsorbed on the  $\text{LaMnO}_{3+\delta}$  surface. Kaddouri et al. [46] reported that  $\text{LaMnO}_{3.15}$  could be reduced to a stoichiometric compound at ca. 550 °C, and the  $\text{H}_2$  consumption was 1.04 mmol/g, higher than that (0.61 mmol/g) estimated according to a  $\delta$  value

of 0.15 ( $\text{LaMnO}_{3+\delta} + \delta\text{H}_2 \rightarrow \text{LaMnO}_3 + \delta\text{H}_2\text{O}$ ). Furthermore, Zhu et al. [47] pointed out that the  $\text{La}_{0.5}\text{Sr}_{0.5}\text{MnO}_3$  single-crystal cubes and particles showed a  $\text{H}_2$  consumption of 3.21–3.23 mmol/g below 600 °C, and the authors assigned the reduction peak at 350 °C to the reduction of  $\text{Mn}^{4+}$  to  $\text{Mn}^{3+}$  and/or to a single-electron reduction of  $\text{Mn}^{3+}$  located in a highly coordination unsaturated microenvironment, the one at 430 or 450 °C to a single-electron reduction of  $\text{Mn}^{3+}$  located in a coordination-unsaturated microenvironment, and the small one (or shoulder) at ca. 200 °C to the removal of the non-stoichiometric excess oxygen accommodated within the lattice. Therefore, the reduction peaks at 393–418 °C of our porous  $\text{LaMnO}_3$  catalysts could be reasonably attributed to the single-electron reduction of  $\text{Mn}^{3+}$  located in a coordination-unsaturated microenvironment. That is to say, the partial reduction of the  $\text{Mn}^{3+}$  species in  $\text{LaMnO}_3$  led to the enhancement in  $\text{H}_2$  consumption. It is apparent that the low-temperature  $\text{H}_2$  consumption of the 3DOM-structured  $\text{LaMnO}_3$  samples was much larger than that of the bulk nonporous  $\text{LaMnO}_3$  sample. Furthermore, the 3DOM-structured  $\text{LaMnO}_3$  samples with higher surface areas consumed more amounts of  $\text{H}_2$  during the reduction process in the low-temperature region.

It has been generally accepted that the low-temperature reducibility of a catalyst can be conveniently evaluated by using the initial (where less than 25% oxygen in the sample was removed for the first reduction band)  $\text{H}_2$  consumption rate [48,49]. Fig. 5B shows the initial  $\text{H}_2$  consumption rate as a function of inverse temperature of the as-prepared  $\text{LaMnO}_3$  samples. It is clearly seen that the initial  $\text{H}_2$  consumption rates of the samples decreased in the order of  $\text{LaMnO}_3\text{-PL-2} > \text{LaMnO}_3\text{-PL-1} > \text{LaMnO}_3\text{-PL-3} > \text{LaMnO}_3\text{-PEG} > \text{LaMnO}_3\text{-MeOH} > \text{LaMnO}_3\text{-bulk}$  as well as  $\text{LaMnO}_3\text{-PL-2} > \text{LaMnO}_3\text{-PL-2.850} > \text{LaMnO}_3\text{-PL-2.950} > \text{LaMnO}_3\text{-bulk}$ . Such trends in low-temperature reducibility were in good consistence with the sequences of catalytic performance shown below.

#### 3.4. Catalytic activity

When only quartz sands were loaded into the microreactor, we did not detect significant conversion of toluene below 400 °C. This result indicates that no homogeneous reactions took place under the adopted reaction conditions. Fig. 6 shows the catalytic activities of the as-prepared  $\text{LaMnO}_3$  samples for the combustion of



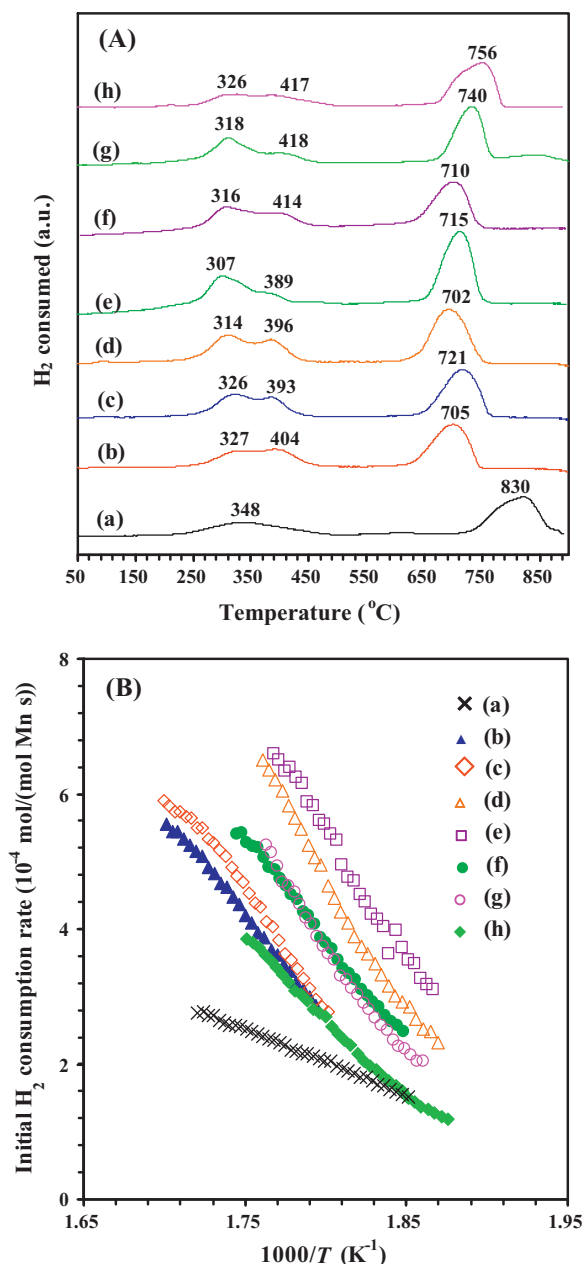


**Fig. 5.** (A) H<sub>2</sub>-TPR profiles and (B) initial H<sub>2</sub> consumption rate as a function of inverse temperature of (a) LaMnO<sub>3</sub>-bulk, (b) LaMnO<sub>3</sub>-MeOH, (c) LaMnO<sub>3</sub>-PEG, (d) LaMnO<sub>3</sub>-PL-1, (e) LaMnO<sub>3</sub>-PL-2, (f) LaMnO<sub>3</sub>-PL-3, (g) LaMnO<sub>3</sub>-PL-2.850, and (h) LaMnO<sub>3</sub>-PL-2.950.

toluene. Obviously, toluene conversion and toluene consumption rate ( $\mu\text{mol}/(\text{g s})$ ) increased with a rise in reaction temperature, and the porous LaMnO<sub>3</sub> catalysts performed much better than the bulk counterpart. It is noted that toluene was completely oxidized to CO<sub>2</sub> and H<sub>2</sub>O over our as-prepared LaMnO<sub>3</sub> catalysts, and there was no detection of incomplete oxidation products, as substantiated by the good carbon balance (ca. 99.5%) in each run. The reaction temperatures  $T_{10\%}$ ,  $T_{50\%}$ , and  $T_{90\%}$  (corresponding to toluene conversion = 10, 50, and 90%) are usually used to evaluate the catalytic activities of samples. Table 2 summarizes the catalytic performance of the as-prepared LaMnO<sub>3</sub> samples. It is seen that among these LaMnO<sub>3</sub> samples, the 3DOM-structured LaMnO<sub>3</sub>-PL-2 sample performed the best, with the  $T_{50\%}$  and  $T_{90\%}$  being ca. 226 and 249 °C, respectively, whereas the bulk LaMnO<sub>3</sub> catalyst gave a  $T_{50\%}$  of ca. 267 °C and a  $T_{90\%}$  of ca. 298 °C; the

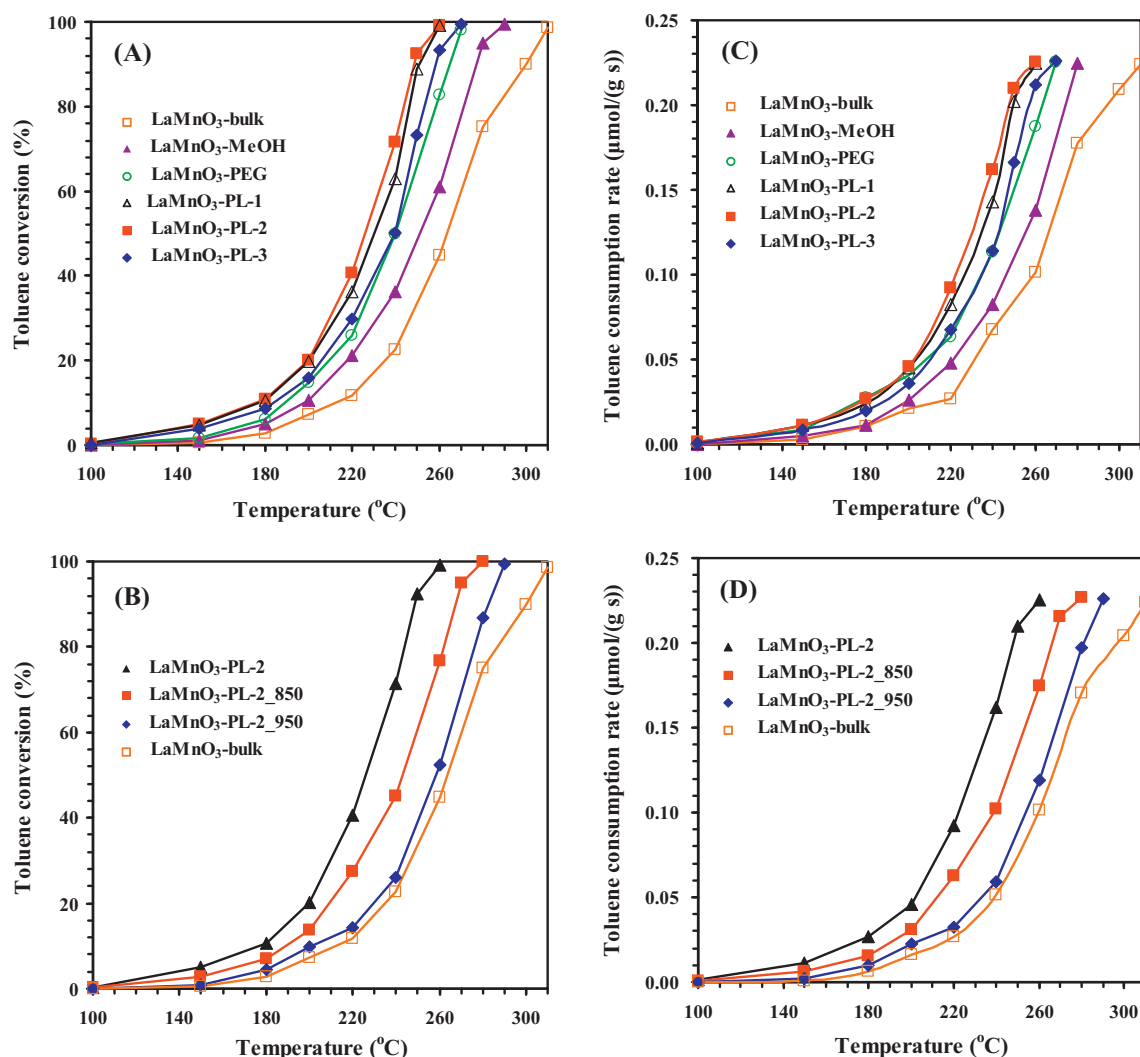
other porous LaMnO<sub>3</sub> catalysts also outperformed the LaMnO<sub>3</sub>-bulk catalyst. Raising the calcination temperature from 750 to 850 or 950 °C caused the LaMnO<sub>3</sub>-PL-2 catalyst to decrease in activity, a result due to the deterioration of the 3DOM structure induced by the growth of LaMnO<sub>3</sub> crystallites, as confirmed by the remarkable drop in surface area from 37.8 m<sup>2</sup>/g (calcined at 750 °C) to 18.8 m<sup>2</sup>/g (calcined at 850 °C) or to 10.1 m<sup>2</sup>/g (calcined at 950 °C). Therefore, it is concluded that the catalytic performance decreased in the sequences of LaMnO<sub>3</sub>-PL-2 > LaMnO<sub>3</sub>-PL-1 > LaMnO<sub>3</sub>-PL-3 > LaMnO<sub>3</sub>-PEG > LaMnO<sub>3</sub>-MeOH > LaMnO<sub>3</sub>-bulk and of LaMnO<sub>3</sub>-PL-2 > LaMnO<sub>3</sub>-PL-2.850 > LaMnO<sub>3</sub>-PL-2.950 > LaMnO<sub>3</sub>-bulk (Fig. 6 and Table 2), coinciding with the orders of low-temperature reducibility revealed by the H<sub>2</sub>-TPR investigations.

Fig. 7 shows the effects of SV and toluene/O<sub>2</sub> molar ratio on the catalytic activity of the LaMnO<sub>3</sub>-PL-2 sample. It is observed that the catalytic activity of LaMnO<sub>3</sub>-PL-2 decreased with increasing the SV value (Fig. 7A) or the toluene/O<sub>2</sub> molar ratio (Fig. 7B). Apparently, the rise in O<sub>2</sub> concentration of the reactant feed favored the enhancement of toluene conversion, suggesting that the oxygen adspecies might play an important role in the combustion of toluene. That is to say, the oxygen nonstoichiometry relevant to structural defects might be a critical factor in determining the catalytic activity of LaMnO<sub>3</sub>. To examine the catalytic stability of the LaMnO<sub>3</sub>-PL-2 sample, we carried out the on-stream reaction experiment at 250 °C and the result is shown in Fig. 8. It is found that there was no significant drop in catalytic activity within 48 h of on-stream reaction. Hence, we believe that the 3DOM-structured LaMnO<sub>3</sub>-PL-2 sample was catalytically durable.

The combustion of toluene has been studied over various catalysts in the past years. Among the LaMnO<sub>3</sub> catalysts prepared in the present investigation, the 3DOM-structured LaMnO<sub>3</sub>-PL-2 catalyst showed the best catalytic performance ( $T_{50\%} = 226$  °C and  $T_{90\%} = 249$  °C at SV = 20,000 mL/(g h);  $T_{50\%} = 243$  °C and  $T_{90\%} = 267$  °C at SV = 40,000 mL/(g h)), which was much better than that ( $T_{50\%} = 254$  °C and  $T_{90\%} = 295$  °C at SV = 178 h<sup>-1</sup>) over LaMnO<sub>3</sub> [9], that ( $T_{50\%} = 279$  °C and  $T_{90\%} = 306$  °C at SV = 178 h<sup>-1</sup>) over LaCoO<sub>3</sub> [9], and that ( $T_{50\%} = 270$  °C and  $T_{90\%} = 300$  °C at SV = 186 h<sup>-1</sup>) over 5 wt% Au/CeO<sub>2</sub> [50], similar to that ( $T_{90\%} = 250$  °C at SV = 18,000 mL/(g h)) over 0.5 wt% Pd/LaMnO<sub>3</sub> [51], but inferior to that ( $T_{50\%} = 202$  °C and  $T_{90\%} = 221$  °C at SV = 20,000 mL/(g h)) over La<sub>0.8</sub>Sr<sub>0.2</sub>MnO<sub>3</sub> [2].

It is well-known that the activity of an ABO<sub>3</sub> catalyst is related to several factors, such as defect nature and density, oxygen adspecies concentration, reducibility, and surface area [52,53]. For the combustion of organics, the catalyst with a higher surface area could show a better catalytic activity [52,53]. To assess the effect of surface area on catalytic activity of the as-prepared catalyst, we calculated the specific rate ( $\mu\text{mol}/(\text{m}^2 \text{ h})$ ) normalized per surface area (Fig. S8). Although the specific rates over the LaMnO<sub>3</sub>-bulk and LaMnO<sub>3</sub>-PL-3.950 catalysts with low surface areas were higher than those over the 3DOM LaMnO<sub>3</sub> catalysts with higher surface areas at the same reaction temperature, the temperatures required for toluene complete oxidation over the 3DOM LaMnO<sub>3</sub> catalysts were lower than those over the LaMnO<sub>3</sub>-bulk and LaMnO<sub>3</sub>-PL-3.950 catalysts (Fig. 6). It means that in addition to surface area, there were other factors that would have an important influence on the catalytic performance of the as-prepared LaMnO<sub>3</sub> samples. In an ABO<sub>3</sub> catalyst, the formation of oxygen vacancies is beneficial for the activation of O<sub>2</sub> molecules to active oxygen adspecies. The oxygen adspecies are usually O<sub>2</sub><sup>-</sup>, O<sub>2</sub><sup>2-</sup> or O<sup>-</sup>. The formation of the electrophilic oxygen (especially O<sup>-</sup>) species would be beneficial for the oxidation of toluene. It has been generally believed that the electrophilic O<sub>ads</sub> species are responsible for the deep oxidation of organics, whereas the nucleophilic oxygen (O<sup>2-</sup><sub>latt</sub>) species account for the selective (partial) oxidation of organics [6,54]. As we know,





**Fig. 6.** Toluene conversion (A and B) and toluene consumption rate (C and D) as a function of reaction temperature over the as-prepared  $\text{LaMnO}_3$  catalysts under the conditions of toluene concentration = 1000 ppm, toluene/oxygen molar ratio = 1/400, and SV = 20,000 mL/(g h).

on one hand, the  $\text{O}_{\text{ads}}$  species on a perovskite surface are mainly  $\text{O}^-$  species, which locate at the structural defects of a perovskite. Among these kinds of oxygen adspecies, the  $\text{O}^-$  species show the highest reactivity towards organic molecules [6,54]. Therefore, a higher  $\text{O}_{\text{ads}}$  species content of  $\text{ABO}_3$  can give rise to a better catalytic performance [54,55]. On the other hand, a good reducibility of  $\text{ABO}_3$  can facilitate the redox process of B-site ions with multiple oxidation states, and hence promoting the oxidation of organics [56]. Compared to the  $\text{LaMnO}_3$ -bulk sample, the 3DOM-structured  $\text{LaMnO}_3$ -PL-2 sample possessed much smaller particle size, higher

surface area, higher surface oxygen species and surface  $\text{Mn}^{4+}$  content, and much better low-temperature reducibility (Figs. 1–5 and Figs. S5, and S6 as well as Tables 1 and 2). Such features of the 3DOM-structured  $\text{LaMnO}_3$ -PL-2 sample contribute to its much better performance in catalyzing the combustion of toluene. Therefore, we conclude that the large surface area, high-quality 3DOM structure with mesoporous skeletons, high oxygen adspecies content, and good low-temperature reducibility might account for the good catalytic activity of the  $\text{LaMnO}_3$ -PL-2 sample for toluene combustion.

**Table 3**  
Rate constants ( $k$ ), pre-exponential factors ( $A$ ), activation energies ( $E_a$ ), and correlation coefficients ( $R^2$ ) of the plot  $\ln k$  versus inverse temperature for the oxidation of toluene over the as-prepared  $\text{LaMnO}_3$  catalysts in the temperature range of 100–200 °C.

Catalyst	$k$ (s <sup>-1</sup> )				$A$ (s <sup>-1</sup> )	$E_a$ (kJ/mol)	$R^2$
	100 °C	150 °C	180 °C	200 °C			
$\text{LaMnO}_3$ -bulk	$1.07 \times 10^{-4}$	$4.43 \times 10^{-3}$	$2.85 \times 10^{-2}$	$7.72 \times 10^{-2}$	$4.25 \times 10^9$	97	0.998
$\text{LaMnO}_3$ -MeOH	$8.61 \times 10^{-4}$	$1.26 \times 10^{-2}$	$5.38 \times 10^{-2}$	$1.18 \times 10^{-1}$	$1.17 \times 10^7$	72	0.998
$\text{LaMnO}_3$ -PEG	$1.90 \times 10^{-3}$	$1.82 \times 10^{-2}$	$6.56 \times 10^{-2}$	$1.74 \times 10^{-1}$	$2.32 \times 10^6$	65	0.995
$\text{LaMnO}_3$ -PL-1	$4.42 \times 10^{-3}$	$5.05 \times 10^{-2}$	$1.20 \times 10^{-1}$	$2.49 \times 10^{-1}$	$7.31 \times 10^5$	58	0.997
$\text{LaMnO}_3$ -PL-2	$4.82 \times 10^{-3}$	$5.28 \times 10^{-2}$	$1.33 \times 10^{-1}$	$2.52 \times 10^{-1}$	$6.55 \times 10^5$	59	0.996
$\text{LaMnO}_3$ -PL-3	$2.81 \times 10^{-3}$	$3.96 \times 10^{-2}$	$9.39 \times 10^{-2}$	$1.88 \times 10^{-1}$	$1.20 \times 10^6$	61	0.994
$\text{LaMnO}_3$ -PL-2.850	$1.90 \times 10^{-3}$	$2.88 \times 10^{-2}$	$7.43 \times 10^{-2}$	$1.57 \times 10^{-1}$	$2.12 \times 10^6$	64	0.996
$\text{LaMnO}_3$ -PL-2.950	$4.75 \times 10^{-4}$	$9.08 \times 10^{-3}$	$5.21 \times 10^{-2}$	$1.10 \times 10^{-1}$	$9.65 \times 10^7$	81	0.998

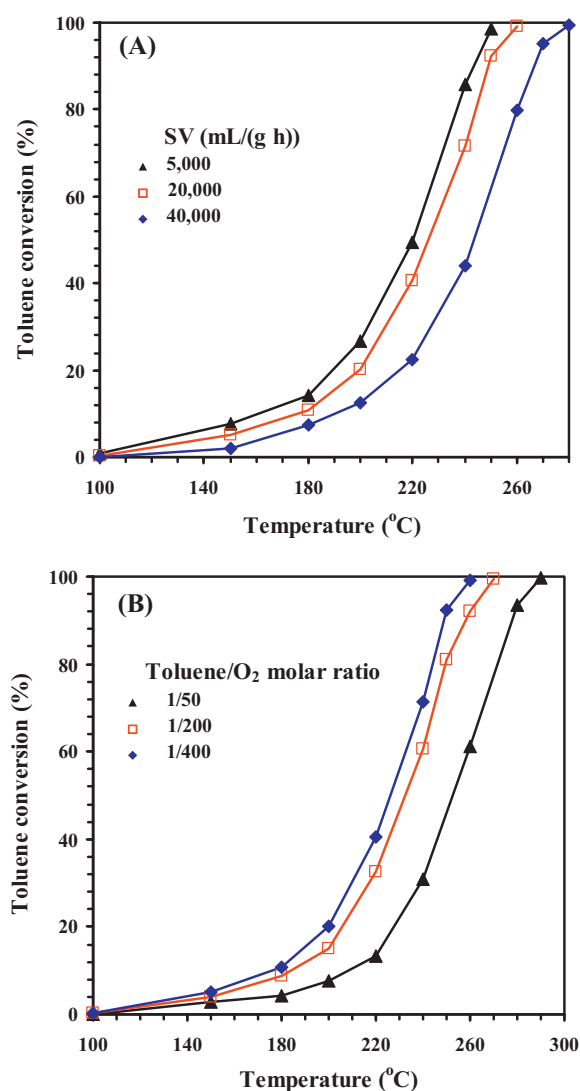


**Fig. 7.** Catalytic activity of the LaMnO<sub>3</sub>-PL-2 sample versus reaction temperature (A) at toluene concentration = 1000 ppm, toluene/O<sub>2</sub> molar ratio = 1/400, and different SV values; and (B) at toluene concentration = 1000 ppm, SV = 20,000 mL/(g h), and various toluene/O<sub>2</sub> molar ratios.

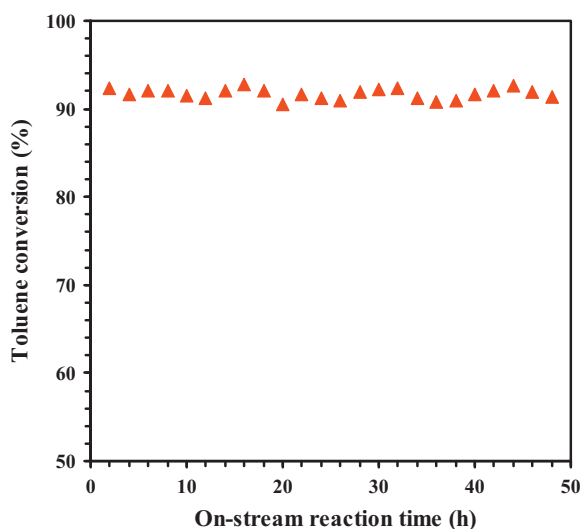


**Fig. 8.** Catalytic activity as a function of on-stream reaction time over the LaMnO<sub>3</sub>-PL-2 sample for toluene oxidation under the conditions of toluene concentration = 1000 ppm, toluene/O<sub>2</sub> molar ratio = 1/400, reaction temperature = 250 °C, and SV = 20,000 mL/(g h).

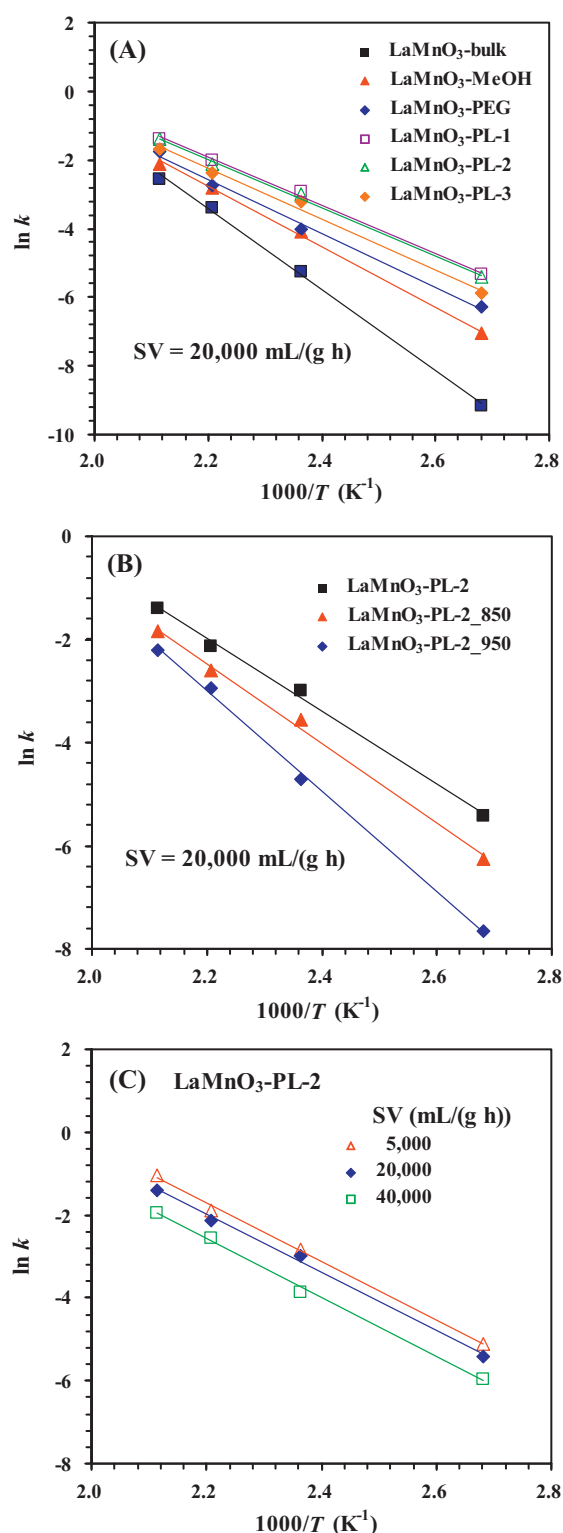


**Fig. 9.** Arrhenius plots for the oxidation of toluene over the LaMnO<sub>3</sub> catalysts.

### 3.5. Kinetic parameters

The kinetics of catalytic oxidation of VOCs has received much attention. Several reports related to the catalytic kinetic behaviors of VOC combustion can be seen in the literature. For instance, the oxidation of butyl acetate over the AgZSM-5 catalyst was proven to be first-order toward butyl acetate concentration and zero-order toward oxygen concentration [57]. Good linear Arrhenius

plots were obtained over ceria–zirconia-supported  $\text{LaCoO}_3$  catalysts for toluene combustion when the reaction was first-order and zero-order kinetics with respect to toluene and oxygen [58], respectively. Hence, it can be reasonably assumed that in the case of excessive oxygen, toluene oxidation would obey a first-order reaction mechanism with respect to toluene concentration ( $c$ ,  $\mu\text{mol/g}$ ):  $r = -kc = (-A \exp(-E_a/RT))c$ , where  $r$  is the reaction rate ( $\mu\text{mol}/(\text{g s})$ ),  $k$  the rate constant ( $\text{s}^{-1}$ ),  $A$  the pre-exponential factor, and  $E_a$  the apparent activation energy ( $\text{kJ/mol}$ ). The  $k$  values could be calculated from the reaction rates and reactant conversions at different SV and reaction temperatures.

Shown in Fig. 9 are the Arrhenius plots for the oxidation of toluene at toluene conversion <20% (at which the reaction temperature was in the range of 100–200 °C) over the as-prepared  $\text{LaMnO}_3$  catalysts. Excellent linear relationships (the correlation coefficients ( $R^2$ ) were rather close to 1) of  $\ln k$  versus  $1000/T$  for all of the  $\text{LaMnO}_3$  catalysts were obtained (Fig. 9A–C). The  $k$ ,  $A$ , and  $E_a$  values for toluene oxidation over these catalysts could be estimated according to the slopes of the Arrhenius plots, and the results are listed in Table 3. It is observed that for each catalyst, the  $k$  value increased with the rise in temperature; at the same temperature, however, the  $k$  values for the 3DOM-structured  $\text{LaMnO}_3$  catalysts were much higher than that for the bulk  $\text{LaMnO}_3$  catalyst (despite its  $A$  value was the highest), and the highest  $k$  value at each temperature was achieved over the 3DOM-structured  $\text{LaMnO}_3$ -PL-2 catalyst (despite its  $A$  value was lower). The  $E_a$  value (97 kJ/mol) of the bulk  $\text{LaMnO}_3$  catalyst was much higher than those (58–81 kJ/mol) of the porous  $\text{LaMnO}_3$  catalysts, in which the 3DOM-structured  $\text{LaMnO}_3$ -PL-1–3 catalysts possessed the lowest  $E_a$  values.

By comparing the  $E_a$  values of different catalysts, one can evaluate their catalytic performance. The lower the  $E_a$  value, the easier is the complete oxidation of organics over a catalyst, and hence the better is the performance of the catalyst. The discrepancy between the  $E_a$  values of the as-prepared catalysts might be due to the differences in pore structure, oxygen nonstoichiometry, and reducibility of the mesopore-walled 3DOM  $\text{LaMnO}_3$  and bulk  $\text{LaMnO}_3$  samples. In the case of toluene combustion, the apparent activation energies (58–61 kJ/mol) obtained over our 3DOM-structured  $\text{LaMnO}_3$ -PL-1–3 catalysts were close to or slightly lower than those (51–79 kJ/mol) over the  $\text{LaCoO}_3/\text{Ce}_{1-x}\text{Zr}_x\text{O}_2$  ( $x=0-0.2$ ) catalysts [58] and that (62 kJ/mol) over the  $\text{Pt}/\text{Ce}_{0.64}\text{Zr}_{0.15}\text{Bi}_{0.21}\text{O}_{1.895}/\text{Al}_2\text{O}_3$  catalyst [59], but much lower than those (120–144 kJ/mol) over the  $\text{CuO}/\text{Al}_2\text{O}_3$  and  $\text{MnO}/\text{Al}_2\text{O}_3$  catalysts [60] and (73–89 kJ/mol) over the Ni- or Mn-doped  $\text{Fe}_3\text{O}_4$  catalysts [61]. Therefore, the results of kinetic investigations confirm that the 3DOM-structured  $\text{LaMnO}_3$  catalysts showed good catalytic performance for the combustion of toluene at low temperatures.

#### 4. Conclusions

3DOM-structured perovskite-type oxides  $\text{LaMnO}_3$  with mesoporous skeletons could be prepared using the PEG- and/or L-lysine-aided PMMA-templating approach. All of the as-prepared  $\text{LaMnO}_3$  samples were single-phase and of rhombohedral crystal structure. The introduction of certain amounts of PEG400 and L-lysine was favorable for the formation of  $\text{LaMnO}_3$  with high-quality 3DOM architecture, mesoporous skeletons, and large surface areas (32–38  $\text{m}^2/\text{g}$ ). Among the  $\text{LaMnO}_3$  samples, the  $\text{LaMnO}_3$ -PL-2 one showed the highest surface area and surface  $\text{Mn}^{4+}$  and adsorbed oxygen species contents; furthermore, the 3DOM-structured  $\text{LaMnO}_3$  samples possessed much better low-temperature reducibility than the bulk counterpart, and the  $\text{LaMnO}_3$ -PL-2 sample was the best in terms of low-temperature reducibility. Under the conditions of toluene

concentration = 1000 ppm, toluene/ $\text{O}_2$  molar ratio = 1/400, and SV = 20,000  $\text{mL}/(\text{g h})$ , the porous  $\text{LaMnO}_3$  catalysts were much superior to the bulk  $\text{LaMnO}_3$  catalyst in activity; over the best-performing  $\text{LaMnO}_3$ -PL-2 catalyst, the  $T_{50\%}$  and  $T_{90\%}$  values were ca. 226 and 249 °C, respectively. The result of kinetic studies reveal that the apparent activation energies (58–61 kJ/mol) for toluene combustion over the  $\text{LaMnO}_3$ -PL-1–3 catalysts were much lower than that (97 kJ/mol) over the bulk  $\text{LaMnO}_3$  catalyst. We believe that the good catalytic performance of the 3DOM-structured  $\text{LaMnO}_3$  with mesoporous skeletons for toluene combustion was associated with the large surface area, high oxygen adspecies content, good low-temperature reducibility, and unique bimodal pore structure.

#### Acknowledgements

The work described was supported by the NSF of China (20973017 and 21077007), the Creative Research Foundation of Beijing University of Technology (00500054R4003 and 005000543111501), “863” Key Program of Ministry of Science and Technology of China (2009AA063201), and the Funding Project for Academic Human Resources Development in Institutions of Higher Learning under the Jurisdiction of Beijing Municipality (PHR201007105 and PHR201107104). We also thank Prof. Chak Tong Au (Department of Chemistry, Hong Kong Baptist University) and Mrs. Jianping He (State Key Laboratory of Advanced Metals and Materials, University of Science & Technology, Beijing) for doing the XPS and SEM analyses, respectively.

#### Appendix A. Supplementary data

Supplementary data associated with this article can be found, in the online version, at doi:10.1016/j.apcatb.2012.02.010.

#### References

- [1] I. Filella, J. Peñuelas, *Atmos. Environ.* 40 (2006) 7752–7769.
- [2] V. Blasin-Aubé, J. Belkouch, L. Monceaux, *Appl. Catal. B* 43 (2003) 175–186.
- [3] J.G. Deng, Y. Zhang, H.X. Dai, L. Zhang, H. He, C.T. Au, *Catal. Today* 139 (2008) 82–87.
- [4] J. Blanco, A.L. Petre, M. Yates, M.P. Martin, J.A. Martin, M.A. Martin-Luengo, *Appl. Catal. B* 73 (2007) 128–134.
- [5] J.-M. Giraudon, A. Elhachimi, F. Wyrwalski, S. Siffert, A. Aboukais, J.-F. Lamonier, G. Leclercq, *Appl. Catal. B* 75 (2007) 157–166.
- [6] L.G. Tejuca, J.L.G. Fierro (Eds.), *Properties and Applications of Perovskite-type Oxides*, Marcel Dekker, New York, 1993.
- [7] H. Najjar, H. Batis, *Appl. Catal. A* 383 (2010) 192–201.
- [8] R. Spinicci, M. Faticanti, P. Marini, S. De Rossi, P. Porta, *J. Mol. Catal. A* 197 (2003) 147–155.
- [9] S. Irusta, M.P. Pina, M. Menéndez, J. Santamaría, *J. Catal.* 179 (1998) 400–412.
- [10] J.G. Deng, L. Zhang, H.X. Dai, H. He, C.T. Au, *Ind. Eng. Chem. Res.* 47 (2008) 8175–8183.
- [11] P. Ciambelli, S. Cimino, S.-D. Rossi, M. Faticanti, L. Lisi, G. Minelli, I. Pettiti, P. Porta, G. Russo, M. Turco, *Appl. Catal. B* 24 (2000) 243–253.
- [12] A. Machocki, T. Ioannides, B. Stasinska, W. Gac, G. Avgouropoulos, D. Delimaris, W. Grzegorzczak, S. Pasieczna, *J. Catal.* 227 (2004) 282–296.
- [13] J.N. Kuhn, U.S. Ozkan, *J. Catal.* 253 (2008) 200–211.
- [14] R.Z. Hou, P. Ferreira, P.M. Vilarinho, *Chem. Mater.* 21 (2009) 3536–3541.
- [15] X.X. Fan, Y. Wang, X.Y. Chen, L. Gao, W.J. Luo, Y.P. Yuan, Z.S. Li, T. Yu, J.H. Zhu, Z.G. Zou, *Chem. Mater.* 22 (2010) 1276–1278.
- [16] M. Sadakane, T. Asanuma, J. Kubo, W. Ueda, *Chem. Mater.* 17 (2005) 3546–3551.
- [17] M. Sadakane, T. Horiuchi, N. Kato, C. Takahashi, W. Ueda, *Chem. Mater.* 19 (2007) 5779–5785.
- [18] Y.N. Kim, S.J. Kim, E.K. Lee, E.O. Chi, N.H. Hur, C.S. Hong, *J. Mater. Chem.* 14 (2004) 1774–1777.
- [19] Y.C. Wei, J. Liu, Z. Zhao, Y.S. Chen, C.M. Xu, A.J. Duan, G.Y. Jiang, H. He, *Angew. Chem. Int. Ed.* 50 (2011) 2326–2329.
- [20] J.F. Xu, J. Liu, Z. Zhao, J.X. Zheng, G.Z. Zhang, A.J. Duan, G.Y. Jiang, *Catal. Today* 153 (2010) 136–142.
- [21] Y.G. Wang, J.W. Ren, Y.Q. Wang, F.Y. Zhang, X.H. Liu, Y. Gao, G.Z. Lu, *J. Phys. Chem. C* 112 (2008) 15293–15298.
- [22] G.Z. Wang, L. Zhang, H.X. Dai, J.G. Deng, C.X. Liu, H. He, C.T. Au, *Inorg. Chem.* 47 (2008) 4015–4022.
- [23] C.X. Liu, L. Zhang, J.G. Deng, Q. Mu, H.X. Dai, H. He, *J. Phys. Chem. C* 112 (2008) 19248–19256.
- [24] H.N. Li, L. Zhang, H.X. Dai, H. He, *Inorg. Chem.* 48 (2009) 4421–4434.



- [25] R.Z. Zhang, H.X. Dai, Y.C. Du, L. Zhang, J.G. Deng, Y.S. Xia, Z.X. Zhao, X. Meng, Y.X. Liu, *Inorg. Chem.* 50 (2011) 2534–2544.
- [26] H.Y. Jiang, H.X. Dai, X. Meng, L. Zhang, J.G. Deng, K.M. Ji, *Appl. Catal. B* 105 (2011) 326–334.
- [27] Q. Huang, A. Santoro, J.W. Lynn, R.W. Erwin, J.A. Borchers, J.L. Peng, R.L. Greene, *Phys. Rev. B* 55 (1997) 14987–14999.
- [28] P. Kameli, H. Salamati, M. Hakimi, *J. Alloys Compd.* 463 (2008) 18–24.
- [29] W.F. Chen, J.M. Hong, Y.X. Li, *J. Alloys Compd.* 484 (2009) 846–850.
- [30] T. Striker, J.A. Ruud, *J. Am. Ceram. Soc.* 93 (2010) 2622–2629.
- [31] X. Wei, P. Hug, R. Figi, M. Trottmann, A. Weidenkaff, D. Ferri, *Appl. Catal. B* 94 (2010) 27–37.
- [32] Z. Branković, K. Duriš, A. Radojković, S. Bernik, Z. Jagličić, M. Jagodič, K. Vojisavljević, G. Branković, *J. Sol–Gel Sci. Technol.* 55 (2010) 311–316.
- [33] X.L. Wang, D. Li, C.X. Shi, B. Li, T.Y. Cui, Z.D. Zhang, *Physica B* 405 (2010) 1362–1368.
- [34] Z.A. Hu, Y.Y. Yang, X.L. Shang, H.L. Pang, *Mater. Lett.* 59 (2005) 1373–1377.
- [35] J.R. Niu, J.G. Deng, W. Liu, L. Zhang, G.Z. Wang, H.X. Dai, H. He, X.H. Zi, *Catal. Today* 126 (2007) 420–429.
- [36] E. Arendt, A. Maione, A. Klisinska, O. Sanz, M. Montes, S. Suarez, J. Blanco, P. Ruiz, *Appl. Catal. A* 339 (2008) 1–14.
- [37] Y.J. Zhu, Y.Q. Sun, X.Y. Niu, F.L. Yuan, H.G. Fu, *Catal. Lett.* 135 (2010) 152–158.
- [38] M. Sadakane, T. Horiuchi, N. Kato, K. Sasaki, W. Ueda, *J. Solid State Chem.* 183 (2010) 1365–1371.
- [39] M. Sadakane, C. Takahashi, N. Kato, H. Ogihara, Y. Nodasaka, Y. Doi, Y. Hinatsu, W. Ueda, *Bull. Chem. Soc. Jpn.* 80 (2007) 677–685.
- [40] Z.B. He, S.-H. Yu, J.P. Zhu, *Chem. Mater.* 17 (2005) 2785–2788.
- [41] G.J. Zhang, Z.R. Shen, M. Liu, C.H. Guo, P.C. Sun, Z.Z. Yuan, B.H. Li, D.T. Ding, T.H. Chen, *J. Phys. Chem. B* 110 (2006) 25782–25790.
- [42] W. Buchmann, R. Spezia, G. Tournois, T. Cartailier, J. Tortajada, *J. Mass Spectrom.* 42 (2007) 517–526.
- [43] F. Rogalewicz, Y. Hoppilliard, G. Ohanessian, *Int. J. Mass Spectrom.* 227 (2003) 439–451.
- [44] M.C. Orilall, N.M. Abrams, J. Lee, F.J. Disalvo, U. Wiesner, *J. Am. Chem. Soc.* 130 (2008) 8882–8883.
- [45] H.B. Deng, L. Lin, Y. Sun, C.S. Pang, J.P. Zhuang, P.K. Ouyang, Z.J. Li, S.J. Liu, *Catal. Lett.* 126 (2008) 106–111.
- [46] A. Kaddouri, S. Ifrah, P. Gelin, *Catal. Lett.* 119 (2007) 237–244.
- [47] F. Teng, W. Han, S.H. Liang, B. Gaugeu, R.L. Zong, Y.F. Zhu, *J. Catal.* 250 (2007) 1–11.
- [48] K. Chen, S. Xie, A.T. Bell, E. Iglesia, *J. Catal.* 198 (2001) 232–242.
- [49] H.X. Dai, A.T. Bell, E. Iglesia, *J. Catal.* 221 (2004) 491–499.
- [50] S. Scire, S. Minicò, C. Crisafulli, C. Satriano, A. Pistone, *Appl. Catal. B* 40 (2003) 43–49.
- [51] A. Musialik-Piotrowska, H. Landmesser, *Catal. Today* 137 (2008) 357–361.
- [52] N. Yi, Y. Cao, Y. Su, W.-L. Dai, H.-Y. He, K.-N. Fan, *J. Catal.* 230 (2005) 249–253.
- [53] N. Gunasekaran, S. Saddawi, J.J. Carberry, *J. Catal.* 159 (1996) 107–111.
- [54] M.A. Peña, J.L.G. Fierro, *Chem. Rev.* 101 (2001) 1981–2018.
- [55] J.G. Deng, L. Zhang, H.X. Dai, H. He, C.T. Au, *Appl. Catal. B* 89 (2009) 87–96.
- [56] T. Nakamura, M. Misono, Y. Yoneda, *Chem. Lett.* 10 (1981) 1589–1592.
- [57] C.T. Wong, A.Z. Abdullah, S. Bhatia, *J. Hazard. Mater.* 157 (2008) 480–489.
- [58] M. Alifanti, M. Florea, S. Somacescu, V.I. Pârvulescu, *Appl. Catal. B* 60 (2005) 33–39.
- [59] T. Masui, H. Imadzu, N. Matsuyama, N. Imanaka, *J. Hazard. Mater.* 176 (2010) 1106–1109.
- [60] S.M. Saqer, D.I. Kondarides, X.E. Verykios, *Appl. Catal. B* 103 (2011) 275–286.
- [61] M. Florea, M. Alifanti, V.I. Pârvulescu, D. Mihaila-Tarabasanu, L. Diamandescu, M. Feder, C. Negrila, L. Frunza, *Catal. Today* 141 (2009) 361–366.